Soft Matter

Accepted Manuscript

This article can be cited before page numbers have been issued, to do this please use: E. Mirzahossein, M. Grzelka and D. Bonn, *Soft Matter*, 2025, DOI: 10.1039/D5SM00279F.

ROYAL SOCIETY OF CHEMISTRY

rsc.li/soft-matter-journal

View Article Online
DOI: 10.1039/D5SM00279F

Unveiling Droplet Morphologies: Real-Time Viscosity Mapping Reveals the Physics of Drying Polymer Solutions

Elham Mirzahossein[a], Marion Grzelka[b], and Daniel Bonn*[a]

The drying of polymer solution droplets produces a fascinating array of morphologies, driven by the formation of a gel-like 'skin' at the vapor/liquid interface. While this skin plays a crucial role in shaping the final droplet form, its precise influence has remained elusive. We present a study that combines innovative fluorescence techniques with classical fluid dynamics to provide insights into the effect of skin formation on the macroscopic final structure of the droplet. Using viscosity-sensitive molecular rotors, we achieve unprecedented real-time, spatially-resolved measurements of local viscosity during the drying process. This novel approach allows us to directly observe and quantify skin formation and growth with micrometer-scale precision. Our experiments reveal that the average thickness and spatial non-uniformity of the skin are the key determinants of the final droplet shape. Droplets were investigated under identical ambient conditions and pinned contact lines, varying only the initial contact angle. This approach yields three distinct morphologies: coffee-rings, 'Mexican hats', and snap-through buckled shapes. For initial contact angle around 30°, skin formation initiates at the contact line rather than the apex, explaining the classic coffee-ring effect. For initial contact angle around 55°, a thicker skin forms near the contact line compared to the apex, resulting in a weaker central region. As evaporation proceeds, this non-uniform skin deforms into the characteristic Mexican hat shape. In contrast, surfaces with initial contact angle around 110° produce a thin, uniform skin that undergoes a dramatic snap-through buckling instability. Crucially, we demonstrate that the timing of morphological changes is directly linked to abrupt variations in skin thickness. Our results not only provide a comprehensive understanding of these complex phenomena but also align with and extend recent theoretical predictions by Head. This work bridges the gap between microscopic skin dynamics and macroscopic droplet behavior, offering a new paradigm for controlling deposition patterns in applications ranging from inkjet printing to biomedical assays.

1 Introduction

The evaporation of particle or polymer solutions is a fascinating out-of-equilibrium phenomenon with wide-ranging implications. The presence of particles or polymers dramatically alters the drying process, leading to a rich variety of behaviors such as wrinkling and cracking in drying paint or clay, skin formation on heated milk, and exotic shapes in evaporating colloidal or polymer solution droplets [1,2]. These phenomena stem from the formation of a gel-like 'skin' at the vapor/liquid interface [3,4]. As evaporation progresses, this elastic shell experiences significant capillary stresses, triggering various mechanical instabilities including buckling [1,5,6], wrinkling [7,8], cavity formation [9], and cracking [10–12].

Despite extensive research, fundamental questions persist regarding the onset of skin formation, its temporal evolution, and its impact on drying kinetics [13–16]. The dynamics of skin formation in sessile droplets are particularly complex due to the presence of a contact line. While rapid evaporation in spherical droplets tends to produce a uniform skin, the fixed contact line in sessile droplets generates a strong radial flow towards the edge, resulting in the well-known 'coffee stain effect' [17]. However, the coffee stain is not the only possible deposition pattern. The initial contact angle of a droplet significantly influences the global evaporation rate and the spatial distribution of deposited solute, leading to a wide range of morphologies in polymer-containing sessile droplets, even under identical solute concentrations and ambient conditions [2,18–22]. Mexican hat shapes and snap-through buckling instabilities are among the most frequently observed morphologies. While several experimental studies have investigated this phenomenon, numerical simulations of this complex 3D evaporation problem remain scarce. To our knowledge, Head is the only one to have explored the deformation of elastic shells with identical initial contact angles, demonstrating the crucial role of skin thickness distribution in determining final droplet morphologies [23]. However, these simulations neglected the viscoelastic nature of the droplet and the dynamics of shell formation.

The lack of micrometer-scale rheological measurements throughout the drying process has hindered our understanding of how skin formation directly affects final droplet morphology. In particular, there is a scarcity of experimental data detailing the spatial and temporal initiation of skin formation and its thickness distribution around the droplet. In this study, we address these knowledge gaps by employing fluorescent molecular rotors to monitor local viscosity during the drying process of aqueous dextran solution droplets. These molecular rotors are fluorescent molecules whose intensity and lifetime are highly sensitive to their immediate environment, with both parameters increasing as local viscosity rises [24,25]. By leveraging this property, we provide unprecedented insights into the drying process of sessile polymer solution droplets at both macroscopic and microscopic scales. Our approach allows us to capture skin thickness variations across the droplet over time, revealing heterogeneities in skin thickness and viscosity. Moreover, we observe two distinct mechanical instabili-

[a] Van der Waals-Zeeman Institute, Institute of Physics, University of Amsterdam, 1098XH Amsterdam, The Netherlands; E-mail: d.bonn@uva.nl
[b] Laboratoire Léon Brillouin, Université Paris-Saclay, CEA, CNRS, 91191 Gif-sur-Yvette, France

† Supplementary Information available: Description of the setup to simultaneously measure fluorescence and rheological properties, macroscopic droplet shape analysis, link between fluorescence lifetime and intensity, relation of complex viscosity with fluorescence properties, 3D reconstruction of drying droplets derived from confocal microscopy, fluorescence lifetime gradients within a droplet, evaluation of skin thickness, microscopic droplet shape analysis, inner and outer skin of snap-through buckling.

View Article Online
DOI: 10.1039/D5SM00279F

ties for droplets on and surfaces with initial contact angle 55° and 110°, characterized by abrupt changes in skin thickness around the time of deformation. This comprehensive analysis bridges the gap between microscopic skin dynamics and macroscopic droplet behavior, offering a new paradigm for understanding and controlling deposition patterns in a wide range of applications.

2 Materials and Methods

An aqueous 25 wt% dextran solution ($M_w \sim 110$ kDa) was prepared by dissolving the polymer in ultrapure water. A solution of 4-DASPI (trans-4-[4-(dimethylamino) styryl]-1-methylpyridinium iodide), a water-soluble molecular rotor, in ultrapure water was added to the polymer solution to achieve a concentration of 10^{-5} M[24].This polymer concentration was selected as it closely aligns with those used in previous studies[2,18], while ensuring effective dye dispersion in a low-viscosity solution and facilitating skin formation. Meanwhile, the low dye concentration guarantees sufficient fluorescence intensity while reducing possible influence of molecular rotors on the polymer distribution. Drying experiments were conducted by depositing polymer solution droplets with initial volumes from 1.5 to 2.5 μL on chemically treated glass surfaces with different contact angles. The relative humidity was maintained at a constant level of $50 - 55$ % using a homemade humidity controller (developed based on Ref.[26]).

All measurements were conducted using #1.5H coverslips (Deckgläser) with a thickness of 170 ± 5 μm. To prepare surfaces with an initial contact angle of approximately $30 \pm 5°$, the coverslips were washed with 99% ethanol, thoroughly rinsed with ultrapure water, dried with nitrogen, and then treated in a plasma cleaner for 30 seconds. For surfaces with an initial contact angle of about $55 \pm 5°$, the coverslips were simply rinsed with water and dried with nitrogen. Surfaces exhibiting an initial contact angle of around 110° were created by soaking the coverslips in a 1% (v/v) toluene/trichlorooctylsilane mixture for 15 minutes, followed by rinsing with isopropanol and drying under nitrogen. The glass coverslips were used immediately after preparation.

To examine the macroscopic deformation of the droplet, side-view images of droplets are captured as a function of time using a CCD camera (Stingray).

To measure fluorescence and rheological properties simultaneously, a rheometer head (Anton Paar DSR 502) is mounted on a Zeiss Axiovert 200 M confocal microscope (see Fig. S1). The rheometer is operated in oscillation mode at a small strain of 0.2% and a frequency $\omega = 10$ rad/s using a 25 mm parallel plate geometry with a gap of 1 mm. The initial polymer solution, identical to that used in the drying droplet experiments, is placed under the rheometer geometry. Both rheological and fluorescence properties are recorded simultaneously during evaporation and gelation at a relative humidity of 50 % (see SI for details). The fluorescence lifetime imaging microscopy (FLIM) was conducted using the time-correlated single photon counting (TCSPC) method on a Leica TCS SP8 inverted confocal microscope equipped with a 20x dry objective (NA = 0.75). The nominal z-resolution, based on the selected wavelength, pinhole size, and objective, is estimated to be 2 μm. The 4-DASPI dye was excited at a repetition rate of 40 MHz using the instrument's pulsed 470 nm laser, and emission was collected between 500 and 700 nm. 4-DASPI inside the dextran polymer solution exhibits a multi-exponential decay. Therefore, all fluorescence lifetime measurements of 4-DASPI are amplitude-averaged lifetimes (see SI for details).

Depending on the surface used for drying experiments, different time-lapse and z-stack imaging protocols were employed. We previously demonstrated that 4-DASPI adsorbs onto hydrophobic surfaces (corresponding to an initial contact angle $\theta_{ini} \sim 110°$), resulting in an increased fluorescence lifetime within the first 10 μm from the surface[27]. However, the lifetime reaches a plateau when measured deeper into the liquid. Therefore, z-stack measurements were performed for $20 < z < 180$ μm on surfaces with $\theta_{ini} \sim 55°$ and for $20 < z < 300$ μm on surfaces with $\theta_{ini} \sim 110°$. For surfaces with $\theta_{ini} \sim 30°$, z-stack measurements closer to the surface were feasible, as the dye shows negligible sensitivity to these more hydrophilic surfaces. Therefore, z-stack measurements were performed for $5 < z < 60$ μm.

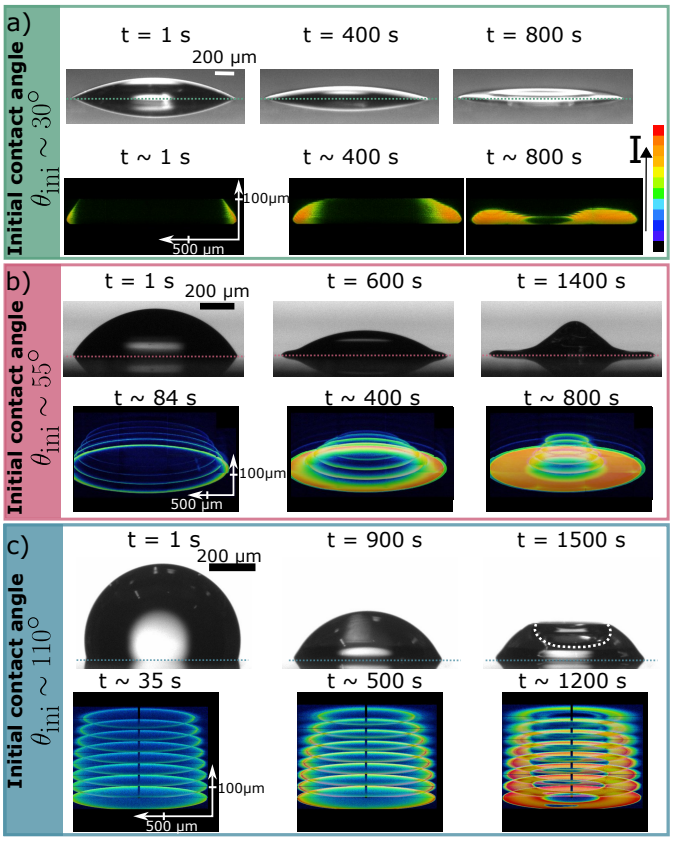

Fig. 1 Sequence of side-view images of bright field and fluorescence intensity images depicting the drying process of a 25 wt % dextran solution droplet on surfaces with initial contact angles (a) $\theta_{ini} \sim 30°$, (b) $\theta_{ini} \sim 55°$ and (c) $\theta_{ini} \sim 110°$. The white dashed line emphasizes the buckled part of the droplet. The colored dashed lines correspond to the solid/liquid interface. Note that microscopic and macroscopic images represent different droplets with slightly varied initial volumes, therefore making direct comparisons of time steps not applicable.

View Article Online
DOI: 10.1039/D5SM00279F

3 Results

3.1 Macroscopic observation

Figure 1 presents side-view images of drying droplets on various surfaces, highlighting the distinct macroscopic deformations of the droplets, which depend on the initial contact angle. The contact line is always pinned for all of the droplets, so that the interfacial properties only influence the initial contact angle and radius of the drop. For polymer droplets on a glass surface with an initial contact angle of 30°, the height of the droplet gradually decreases over time, resulting in a deposition pattern resembling a coffee stain effect at the end of the drying process (see Fig. 1a). However, for polymer droplets on a glass surface with an initial contact angle of 55° (Fig. 1b), the droplet initially undergoes a decrease in height. Subsequently, the droplet's height starts to increase in the center, giving rise to the distinctive Mexican hat shape[18]. In contrast, for a droplet on a surface with an initial contact angle of 110° (Fig. 1c), the dynamics of the droplet shape exhibit distinctly different behavior: upon evaporation of the water, at a certain point, the curvature at the apex of the drop suddenly reverses (white dashed line in Fig.1c). This behavior is indicative of a mechanical instability known as snap-through buckling[20]. The macroscopic droplet shape analysis is provided in SI, Fig. S2. The experiments were conducted with and without the dye: no influence of the dye on the outcome of the experiments was observed.

3.2 Linking the fluorescence of 4-DASPI to the rheological properties

To achieve a microscopic understanding of the drying process of polymer droplets on different surfaces, we first need to correlate the fluorescence properties of 4-DASPI to the macroscopic viscoelastic parameters of the polymer solution. To do so, a droplet of the dextran/4-DASPI solution of the same initial solution as for drying experiment is deposited onto a microscope cover slide. A rheometer head is used to measure the rheological properties of the solution using a parallel-plate geometry while a confocal microscope underneath the cover slide is used to locally measure the fluorescence intensity of 4-DASPI, focusing on the sample's edge where gelation initiates (see inset in Fig. 2a). This approach is used because, in parallel plate geometry, the rheometer primarily captures the most significant contributions to the viscoelastic properties at the sample's edge where the deformation is largest[28]. The parallel plate experiments serve as a calibration system correlating 4-DASPI fluorescence with rheological properties. Since rheometer torque is dominated by the sample edge where shear rates are highest, positioning our confocal measurements at this edge creates direct correspondence between local fluorescence and bulk rheological response. This calibration relationship is then applied to interpret fluorescence measurements in sessile droplets.

The results presented in Fig. 2a enable us to link rheological properties to fluorescence intensity. By using the relationship between fluorescence intensity and a lifetime of 4-DASPI in dextran polymer solutions obtained using FLIM setup (shown in the inset of Fig. 2b), we can also correlate the storage and loss moduli

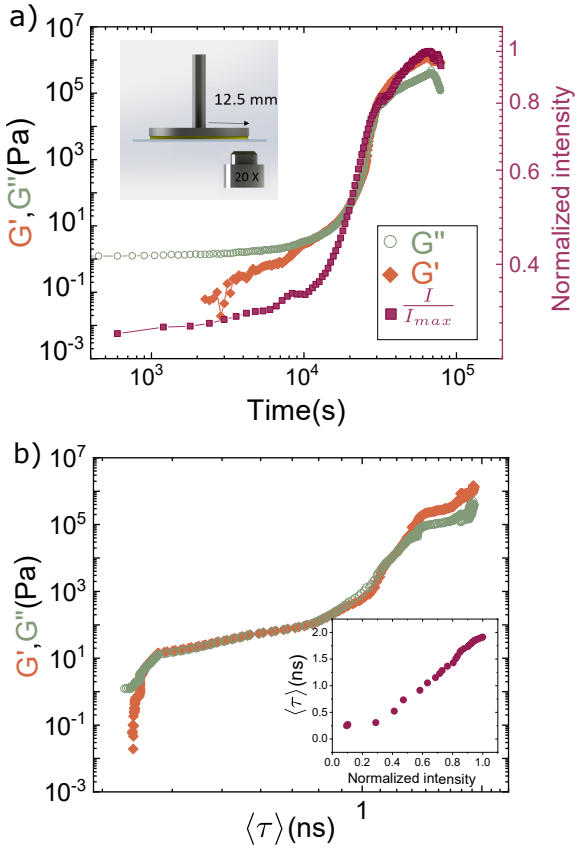

Fig. 2 a) Relationship between the fluorescence intensity of 4-DASPI and the macroscopic viscoelastic properties of the dextran solution. The left axis shows the storage (G') and loss (G'') moduli, while the right axis displays the normalized fluorescence intensity ($\frac{I}{I_{max}}$) as a function of time obtained by confocal microscope. The inset depicts the rheometer and microscope setup. b) Using the relationship between fluorescence lifetime ($\langle\tau\rangle$) and normalized intensity (inset), we correlate G' and G'' with the fluorescence lifetime values.

with the fluorescence lifetime ($\langle\tau\rangle$) shown in Fig.2b. A detailed explanation of the direct correlation between fluorescence intensity and lifetime can be found in SI (see Fig. S3).

During the process of drying, as the solvent within the dextran solution begins to evaporate, both the storage (G') and the loss (G'') moduli increase up to a point where $G' \approx G''$. This point is commonly taken as the sol-gel transition point. Beyond this point, both parameters consistently rise together over time. The confocal measurements show that the increase in normalized fluorescence intensity,($\frac{I}{I_{max}}$) matches the increase of both G' and G''. After approximately 30000 s, G' exceeds G'', after which elasticity dominates in the system. At this point, the formation of the elastic skin begins and the system switches to a predominantly elastic regime which corresponds to an average fluorescence lifetime $\langle\tau\rangle = 1.3 \pm 0.1$ ns. This point is defined as the threshold at which skin formation begins in our system. Moreover, as usually done for viscoelastic materials[29,30], we can correlate the fluorescence lifetime with the complex viscosity $|\eta^*| = \frac{\sqrt{G'^2+G''^2}}{\omega}$ (see Fig. S3 and Fig. S4.).

View Article Online
DOI: 10.1039/D5SM00279F

3.3 Microscopic Investigation: dynamics of skin formation and thickness growth

To investigate the *local* viscoelastic properties of the dextran droplets during the drying process on surfaces exhibiting different initial contact angles, we measure the average fluorescence lifetime of 4-DASPI within the polymer solution as the droplet evaporates. The x-y position is focused on the periphery of the droplet at the vapor/liquid interface. It is crucial to emphasize that, especially in droplet experiments, fluorescence lifetime measurement is preferred over fluorescence intensity. Unlike fluorescence intensity, fluorescence lifetime is independent of dye concentration and is not affected by scattering and absorption effects that attenuate the fluorescence intensity along the z-axis.

3.3.1 Skin formation dynamics

The microscopic 3D reconstruction of the side view of fluorescence intensity confocal images is shown in Fig. 1 and Fig. S5 for droplets on three surfaces. We initially focus on the liquid/vapor interface to examine the potential formation of a skin. There is radial symmetry in the formation of skin within the droplet at every z position. Fig.3 on the left-hand side shows the averaged fluorescence lifetime evolution in time at different z-positions at the liquid/vapor interface. Using the calibration curve (Fig. 2), we can convert all fluorescence lifetime values to the elastic modulus of the polymer solution. Fig.3 on the right-hand side shows the results of this conversion in a spatiotemporal diagram.

For a droplet on a surface with an initial contact angle $\theta_{\text{ini}} \sim 30^\circ$ (Fig. 3a), the fluorescence lifetime increases rapidly within the initial few layers. Therefore, the droplet rapidly gelates at lower z positions ($z = 5, 15, 25$ μm) near the contact line, while the upper layers do not gelate. Instead, these upper layers recede in the z direction due to ongoing evaporation until all the liquid evaporates. Note that the droplet reaches its maximum height between $z = 25$ μm and 45 μm, making it impossible to measure the fluorescence lifetime in higher layers ($z = 45\mu$m and $z = 60$ μm) after 800 seconds. Ultimately, only the coffee stain undergoes complete gelation and no shell forms around the droplet. The white dashed line in Fig. 3 right-hand side represents the elastic-dominant regime (skin formation) defined through rheological measurements, which corresponds to a fluorescence lifetime of 1.3 ns.

For droplets on surfaces with an initial contact angle $\theta_{\text{ini}} \sim 55^\circ$ (Fig. 3b), at the first layer ($z = 20$ μm), $\langle\tau\rangle$ experiences a rapid increase, reaching a saturation point at around 2.0 ± 0.1 ns. Near the top of the droplet, at $z = 180$ μm, the increase occurs more gradually: Initially, at $t = 84$ s after drop-casting, G' remains relatively constant over the z-positions, with G' roughly between 10 and 70 Pa. However, with time, a significant elasticity gradient emerges across different z-positions due to the substantial accumulation of polymers closer to the contact line. This gradient intensifies until a point, where the lowest layer gelates and forms a skin, followed by successive gelation of the other layers from bottom to top as time goes on. Around $t \sim 670$ s, all layers become interconnected due to the formation of a continuous skin around the droplet. However, *the bulk of the droplet remains fully liquid* over this timeframe (see Fig. S7 for $t < 700$ s).

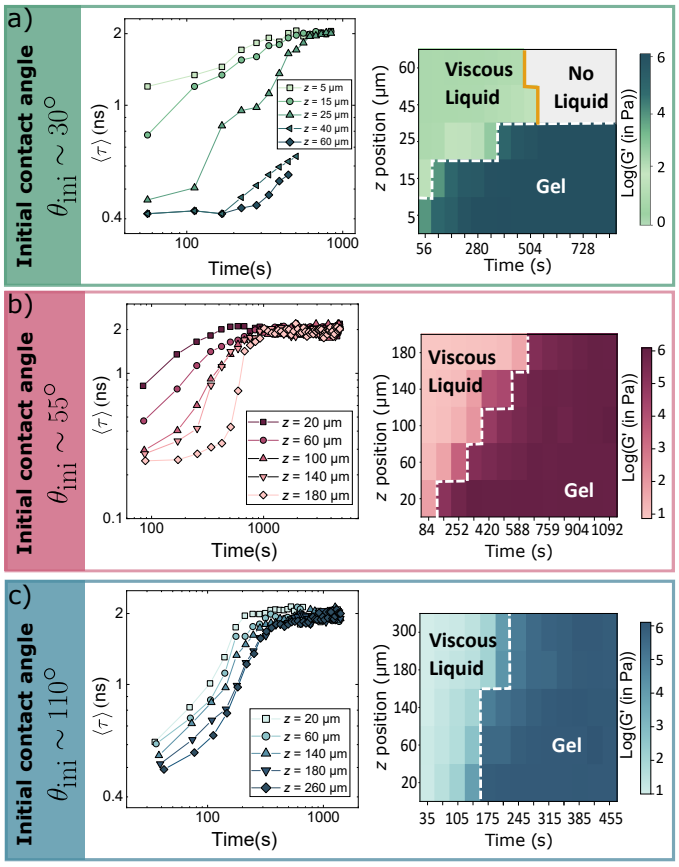

Fig. 3 Average fluorescence lifetime and storage modulus as a function of time across the vapor/liquid interface of a droplet of dextran and 4-DASPI on glass surfaces with initial contact angles (a) $\theta_{\text{ini}} \sim 30^\circ$, (b) $\theta_{\text{ini}} \sim 55^\circ$ and (c) $\theta_{\text{ini}} \sim 110^\circ$. Measurements were taken at various z positions.

In contrast, the dynamics are completely different for the droplets drying on surfaces with an initial contact angle $\theta_{\text{ini}} \sim 110^\circ$ (Fig. 3c). Across all z-positions near the vapor/liquid interface, $\langle\tau\rangle$ exhibits a remarkably smaller variance compared to droplets on surfaces with $\theta_{\text{ini}} \sim 30^\circ$ and 55°. Consequently, all layers form a skin within a relatively narrow time-frame.

3.3.2 Skin thickness dynamics

To estimate the skin thickness (H_s) at a specific time and z position, we measure the fluorescence lifetime across a cross-section of the droplet from the center ($R(z) = 0$) to the periphery ($R_m(z)$) at the vapor/liquid interface (see Fig.4b for definition of $R(z) = 0$ and $R_m(z)$). We define the skin thickness using a fluorescence lifetime threshold of 1.3 ns (as defined earlier), identifying the skin as the region where the fluorescence lifetime is equal to or exceeds this value. Thus, the skin thickness is determined based on this cutoff. Detailed measurement procedures are provided in SI, Fig. S8. The results for surfaces with initial contact angles around 30°, 50° and 110° are presented in Fig. 4a,b, and c, respectively.

For a droplet on a surface with $\theta_{\text{ini}} \sim 30^\circ$ (Fig.4a) the skin thickness $H_s(z)$ smoothly increases in the initial few layers, while no skin forms at the upper layers ($z = 45$ and 60 μm) as

View Article Online
DOI: 10.1039/D5SM00279F

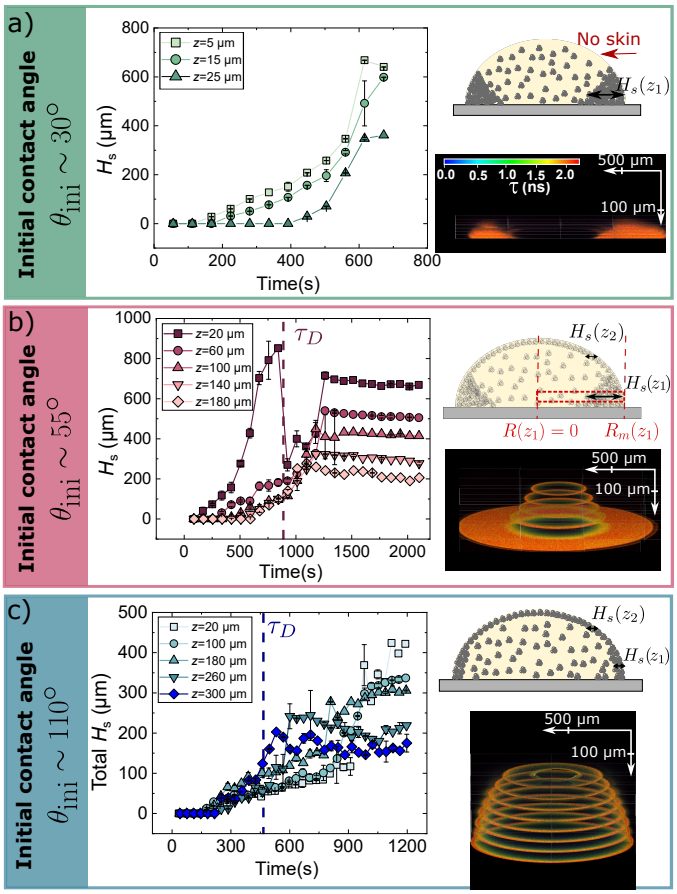

Fig. 4 Skin thickness as a function of time at different z-positions for droplets of dextran and 4-DASPI on surfaces with initial contact angles (a) $\theta_{ini} \sim 30°$, (b) $\theta_{ini} \sim 55°$ and (c) $\theta_{ini} \sim 110°$
. The total H_s is equal to $H_s(inner)+H_s(outer)$. Dashed lines indicate τ_D, the droplet deformation time. Schematic images as well as fluorescence lifetime images illustrate the results in different drying dynamics.

explained above,(see Fig.3a). For dextran droplets on a surface with $\theta_{ini} \sim 55°$, the skin thickness $H_s(z)$ at various z-positions within the droplet gradually increases over time. Notably, there is a substantial difference in skin thickness between the layer near the contact line ($z_1 = 20$ μm), and the layer close to the apex of the droplet ($z_2 = 180$ μm). At a certain point, there is an abrupt change in skin thickness $H_s(z_1 = 20$ μm) and the radius of the cross-section of the droplet which can be seen in Fig. 4b (dark red data points) and Fig. S9, respectively. These changes likely correspond to the abrupt increase of the droplet height, giving birth to a final Mexican hat shape. The time at which this sharp transition occurs is called the deformation time, τ_D. At this point, the droplet undergoes a mechanical instability. This is ascribed to the deformation of the droplet, transitioning from a spherical cap shape to the distinctive "Mexican hat" shape, as shown in Fig. 1b. The drying process continues until full solvent evaporation, eventually resulting in further instabilities like wrinkling and, ultimately, the formation of a cavity within the droplet (see Fig. S6). As shown in Fig. 4c, the trend is significantly different for dextran droplets on surfaces with $\theta_{ini} \sim 110°$. The skin thickness at different z-positions displays a growth pattern up to the point where the apex inverts, the phenomena known as snap-through instabilities. Following this inversion, the top layer experiences a relatively sharp increase in skin thickness, referred to as the deformation time τ_D,(Fig. 4c dark blue data points). After the inversion of the apex, the droplet has inner skin and outer skin. Therefore the total skin is plotted in Fig.4c, which is the sum of the inner and outer skin. The growth patterns of the inner and outer skin are individually illustrated in Fig. S10. As the solvent continues to evaporate, a cavity also forms within the droplet (see Fig. S6).

4 Discussion

The formation of an elastic shell around the droplet does not halt evaporation but rather slows it down, allowing solvent to continue escaping through the shell. As evaporation proceeds, capillary forces develop, causing stresses within the shell that lead to mechanical instabilities. We observed two distinct mechanical instabilities: 1) snap-through buckling, and 2) formation of a "Mexican hat" shape, both intriguingly correlated to the thickness and distribution of the skin around the droplet. To elucidate the difference between these mechanical instabilities, we analyze the average skin thickness over the entire drop $\langle H_s \rangle$ and the dimensionless non-uniformity parameter defined by Head, $\rho = \frac{H_s(z_1)-H_s(z_2)}{H_s(z_1)}$ where z_1 corresponds to the point closer to the contact line and z_2 corresponds to the point closer to the apex[23] (Fig. 4 b and c). When $\rho = 0$, the droplet exhibits uniform shell thickness, whereas for large ρ, the shell becomes thinner closer to the apex relative to the contact line. $\rho = 1$ indicates that $H_s(z_2) = 0$, meaning no skin forms at higher z positions. For droplets on a surface with $\theta_{ini} \sim 30°$, no skin forms at higher z positions, resulting in $\rho = 1$. Consequently, the droplet does not buckle and exhibits the well-known coffee stain effect. For polymer droplets on surfaces with initial contact angle around 55°, the calculated ρ value just before deformation time (τ_D) is approximately 0.91, with an average skin thickness $\langle H_s \rangle = 265$ μm. This indicates a thick shell, thinner near the apex and thicker toward the contact line. Numerical simulations[23] suggest that increasing ρ reduces the buckling pressure of the droplet. For $\rho > 0.7$, the shell is substantially "weaker" compared to an ideal thin elastic shell. Consequently, the shell deforms more significantly near the apex than at the contact line as pressure changes, leading to the formation of a Mexican hat shape. In contrast, polymer droplets on surfaces with $\theta_{ini} \sim 110°$ exhibit a ρ value close to zero (between -0.4 and 0.1 due to thickness measurement uncertainties) just before τ_D, with an average skin thickness $\langle H_s \rangle = 30$ μm. This indicates a thin shell with uniform skin distribution. Numerical simulations[23] predict that for a thin elastic shell with relatively uniform skin thickness (ρ close to zero), capillary pressure increases with further solvent evaporation until reaching a critical pressure. At this point, to minimize the total free energy, the shell discontinuously inverts its spherical surface at the apex, as observed for an ideal elastic shell[31,32]. This results in snap-through buckling.

View Article Online
DOI: 10.1039/D5SM00279F

5 Conclusions

In conclusion, we have conducted a comprehensive investigation into the dynamics of skin formation and growth in evaporating polymer solution droplets, encompassing both microscopic and macroscopic scales. Our study reveals distinct behaviors for droplets on different surfaces: For droplets on surfaces with initial contact angle around 30°, skin formation is localized at the contact line, with no skin developing near the apex. This localized skin formation leads to the well-known coffee stain effect. On surfaces with initial contact angle around 55°, skin formation initiates near the contact line and progresses towards the apex over a significantly longer timescale. This results in a highly non-uniform shell, with skin thickness near the contact line an order of magnitude greater than at the apex. The uneven distribution of skin thickness induces a morphological transition from a spherical cap to a distinctive Mexican hat shape. Further evaporation leads to additional instabilities, including wrinkling and cavity formation within the droplet. In contrast, droplets on surfaces with a high initial contact angle (around 110°) develop a thin shell with uniform skin thickness across the entire surface. This uniformity causes the droplet to behave analogously to an ideal elastic shell, ultimately resulting in snap-through buckling. We have identified that the deformation time (or buckling time) in both scenarios can be precisely determined by measuring abrupt changes in skin thickness at specific z positions. These sudden variations in skin thickness at a given z position are attributed to the migration of the skin to different z positions during the deformation process. Our novel approach, utilizing fluorescent molecular rotors, provides unprecedented insights into the spatiotemporal dynamics of skin formation and its impact on droplet morphology. This method allows for real-time, in situ measurements of local viscosity and skin thickness, revealing the critical role of skin thickness distribution in determining the final droplet shape. These findings not only confirm and extend theoretical predictions but also offer a new paradigm for understanding and controlling deposition patterns in various applications, from inkjet printing to biomedical assays. The observed correlation between skin thickness distribution and mechanical instabilities has significant implications for industrial processes involving drying droplets. For instance, in spray drying applications, controlling the initial contact angle and surface properties could allow for precise tailoring of particle morphology. In inkjet printing, understanding the relationship between skin formation and final droplet shape could lead to improved print quality and resolution. Furthermore, our results shed light on the complex interplay between evaporation kinetics, skin formation, and mechanical instabilities in drying polymer solution droplets. This deeper understanding could pave the way for new strategies in creating functional materials with controlled morphologies, such as hierarchical structures for enhanced catalysis or drug delivery systems with tunable release profiles. Future work could explore the impact of polymer molecular weight, concentration, and solvent properties on skin formation and resulting droplet morphologies. Additionally, extending this methodology to multi-component systems or non-Newtonian fluids could provide valuable insights for a broader range of applications, from food science to advanced materials engineering.

Author contributions

E. M., M. G. and D. B. designed the research; E. M. performed the research; E. M. analyzed the data; and all the authors contributed to the final version of the manuscript.

Conflicts of interest

The authors report no conflicts of interest.

Acknowledgements

This project has received funding from the European Research Council (ERC) under the European Union's Horizon 2020 research and innovation program (Grant agreement No. 833240).

Notes and references

1 N. Tsapis, E. R. Dufresne, S. S. Sinha, C. S. Riera, J. W. Hutchinson, L. Mahadevan and D. A. Weitz, *Physical Review Letters*, 2005, **94**, 018302.
2 L. Pauchard and C. Allain, *Comptes Rendus. Physique*, 2003, **4**, 231–239.
3 P. de Gennes, *The European Physical Journal E*, 2002, **7**, 31–34.
4 T. Okuzono, K. Ozawa and M. Doi, *Physical Review Letters*, 2006, **97**, 136103.
5 J. Zhou, X. Man, Y. Jiang and M. Doi, *Advanced Materials*, 2017, **29**, 1703769.
6 A. Bala Subramaniam, M. Abkarian, L. Mahadevan and H. A. Stone, *Nature*, 2005, **438**, 930–930.
7 D. Riccobelli, H. H. Al-Terke, P. Laaksonen, P. Metrangolo, A. Paananen, R. H. A. Ras, P. Ciarletta and D. Vella, *Physical Review Letters*, 2023, **130**, 218202.
8 C. Seyfert, J. Rodríguez-Rodríguez, D. Lohse and A. Marin, *Physical Review Fluids*, 2022, **7**, 023603.
9 F. Meng, M. Doi and Z. Ouyang, *Physical Review Letters*, 2014, **113**, 098301.
10 B. D. Caddock and D. Hull, *Journal of Materials Science*, 2002, **37**, 825–834.
11 R. Iqbal, A. Q. Shen and A. K. Sen, *Journal of Colloid and Interface Science*, 2020, **579**, 541–550.
12 F. Giorgiutti-Dauphiné and L. Pauchard, *The European Physical Journal E*, 2018, **41**, 32.
13 Y. Shimokawa, T. Kajiya, K. Sakai and M. Doi, *Physical Review E*, 2011, **84**, 051803.
14 G. Du, F. Ye, H. Luo, G. Jing, M. Doi and F. Meng, *Communications in Theoretical Physics*, 2022, **74**, 095605.
15 M. G. Hennessy, G. L. Ferretti, J. T. Cabral and O. K. Matar, *Journal of Colloid and Interface Science*, 2017, **488**, 61–71.
16 L. Talini and F. Lequeux, *Soft Matter*, 2023, **19**, 5835–5845.
17 R. D. Deegan, O. Bakajin, T. F. Dupont, G. Huber, S. R. Nagel and T. A. Witten, *Nature*, 1997, **389**, 827–829.
18 L. Pauchard and C. Allain, *Europhysics Letters*, 2003, **62**, 897.
19 L. Pauchard and C. Allain, *Physical Review E*, 2003, **68**, 052801.

View Article Online
DOI: 10.1039/D5SM00279F

20 Y. Gorand, L. Pauchard, G. Calligari, J. P. Hulin and C. Allain, *Langmuir*, 2004, **20**, 5138–5140.
21 F. Boulogne, F. Giorgiutti-Dauphiné and L. Pauchard, *Soft Matter*, 2013, **9**, 750–757.
22 M. Yu, C. Le Floch-Fouéré, L. Pauchard, F. Boissel, N. Fu, X. D. Chen, A. Saint-Jalmes, R. Jeantet and L. Lanotte, *Colloids and Surfaces A: Physicochemical and Engineering Aspects*, 2021, **620**, 126560.
23 D. A. Head, *Physical Review E*, 2006, **74**, 021601.
24 J. Kim and M. Lee, *The Journal of Physical Chemistry A*, 1999, **103**, 3378–3382.
25 R. Le Dizès Castell, E. Mirzahossein, M. Grzelka, S. Jabbari-Farouji, D. Bonn and N. Shahidzadeh, *The Journal of Physical Chemistry Letters*, 2024, **15**, 628–635.
26 F. Boulogne, *The European Physical Journal E*, 2019, **42**, 51.
27 E. Mirzahossein, M. Grzelka, F. Guerton, D. Bonn and R. Brown, *Scientific Reports*, 2022, **12**, 22197.
28 P. Coussot, *The European Physical Journal B - Condensed Matter and Complex Systems*, 2000, **15**, 557–566.
29 A.-Y. Jee, E. Bae and M. Lee, *The Journal of Chemical Physics*, 2010, **133**, 014507.
30 A. Vyšniauskas, I. López-Duarte, N. Duchemin, T.-T. Vu, Y. Wu, E. M. Budynina, Y. A. Volkova, E. P. Cabrera, D. E. Ramírez-Ornelas and M. K. Kuimova, *Physical Chemistry Chemical Physics*, 2017, **19**, 25252–25259.
31 A. Libai and J. G. Simmonds, *The Nonlinear Theory of Elastic Shells: One Spatial Dimension*, Elsevier, 2012.
32 Yeh Kai-Yuan, Song Wei-Ping and W. L. Cleghorn, *International Journal of Non-Linear Mechanics*, 1994, **29**, 603–611.

View Article Online
DOI: 10.1039/D5SM00279F

Data Availability Statement:

The data that support the findings of this study are available from the corresponding author upon reasonable request.